Single-crystal equations of state of magnesiowüstite at high pressures

GREGORY J. FINKELSTEIN[1,*], JENNIFER M. JACKSON[1,†], WOLFGANG STURHAHN[1], DONGZHOU ZHANG[2], E. ERCAN ALP[3], AND THOMAS S. TOELLNER[3]

[1]Seismological Laboratory, California Institute of Technology, 1200 East California Boulevard, MS 252-21, Pasadena, California 91125, U.S.A.
[2]Partnership for Extreme Crystallography, University of Hawaii, School of Ocean and Earth Science and Technology, 1680 East West Road, Honolulu, Hawaii 96822, U.S.A.
[3]Advanced Photon Source, Argonne National Laboratory, 9700 South Cass Avenue, Argonne, Illinois 60439, U.S.A.

ABSTRACT

Solid solutions of (Mg,Fe)O with high iron enrichment may be an important component of ultralow-velocity zones at Earth's core-mantle boundary. However, to date there have been few high-precision studies on the elastic properties of these materials. In this study we present results on the compression of $(Mg_{0.22}Fe_{0.78})O$ magnesiowüstite in both neon and helium pressure media using single-crystal diffraction to ~55 GPa. In addition, our sample was characterized by time-domain synchrotron Mössbauer spectroscopy at ambient pressure using an extended time range that resulted in vastly improved energy resolution. The combination of these high-resolution techniques tightly constrains the presence of a defect-structure component at room pressure due to 4.7 mol% tetrahedrally coordinated ferric iron, resulting in a renormalized composition of $(Mg_{0.215}Fe_{0.762}\square_{0.023})O$. Both high-pressure diffraction data sets are well described by a third-order Birch-Murnaghan equation of state. The best fit-parameters for a crystal with cubic structure in helium are $K_{0T} = 148(3)$ GPa, $K'_{0T} = 4.09(12)$, and $V_0 = 78.87(6)$ Å^3. Increasing differential stress in the neon-containing sample chamber was correlated with increasing apparent distortion of the initially cubic unit cell, requiring a lower-symmetry hexagonal cell to fit the data above ~20 GPa. For fit equations of state, we determine the pressure-dependent correlation ellipses for the equation of state parameters and compare with previously published single-crystal diffraction data from (Mg,Fe)O crystals in a helium medium. We make two main observations from the data sets using a helium pressure medium: K_{0T} decreases as a function of increasing iron content from periclase to wüstite and K'_{0T} is consistent with an approximately constant value of 4.0 that is independent of iron content, at least up to the iron concentration measured here. In combination with previously reported thermal parameters, we compute the density of magnesiowüstite with this composition at core-mantle boundary conditions and discuss the implications.

Keywords: Magnesiowüstite, single-crystal diffraction, elasticity, equations of state, Mössbauer spectroscopy, high pressure

INTRODUCTION

Ferromagnesian oxides are a primary component of the Earth's lower mantle, along with the dominant bridgmanite and minor CaSiO$_3$ perovskite phases (Irifune 1994; Tschauner et al. 2014). While the bulk of the lower mantle likely contains (Mg,Fe)O ferropericlase solid solutions with ~10–40 mol% of FeO (Fei et al. 1996; Mao 1997; Sinmyo et al. 2008), the presence of material significantly more enriched in Fe has been hypothesized as an explanation for some of the complex seismic structure observed near the core-mantle boundary (CMB). In particular, ultralow-velocity zones (ULVZs), tens of kilometer-thick patches at the CMB, show a ~10% reduction in seismic P-wave velocity and a ~30% reduction in seismic S-wave velocity from average lower-mantle values (Wen 1998; Thorne and Garnero 2004; Rost et al. 2006).

While several suggestions have been put forth in the literature to explain the origin of these features (Manga and Jeanloz 1996; Williams et al. 1998; Mao et al. 2006), one hypothesis that has gained traction in recent years proposes Fe-rich oxide components to explain the observed low sound velocities. Work by Wicks et al. (2010) used nuclear resonant inelastic scattering to show that the shear velocity of $(Mg_{0.16}Fe_{0.84})O$ magnesiowüstite was ~55% slower than end-member MgO at CMB pressures, and that only ~10 vol% of this material mixed with a silicate assemblage would be needed to match ULVZ seismic velocities. Subsequent simulations (Bower et al. 2011) that explored the geodynamic effects of enriching ULVZ material with magnesiowüstite produced morphologies consistent with observed ULVZ seismic topography (Sun et al. 2013).

While selected properties of (Mg,Fe)O with low iron concentrations have been determined at pressures above 1 Mbar and temperatures over 2000 K (Westrenen et al. 2005; Lin et al. 2006, 2007; Mao et al. 2011), until recently, the iron-rich members of this solid solution received less attention (Ohta et al. 2014;

Wicks et al. 2015, 2017), and still little is known about their crystallographic and elastic properties. At ambient conditions, all (Mg,Fe)O solid solutions crystallize in the cubic B1 structure. Single-crystal X-ray diffraction (SXRD) has shown, however, that end-member wüstite, FeO, undergoes a slight rhombohedral distortion from cubic symmetry at ~18–23 GPa and 300 K (Hazen and Jeanloz 1984; Shu et al. 1998; Jacobsen et al. 2005), whereas $(Mg_{0.73}Fe_{0.27})O$ remains cubic to at least 51 GPa (Jacobsen et al. 2005). A powder diffraction (PXRD) study on $(Mg_{0.22}Fe_{0.78})O$ reported a rhombohedral transition at 20–40 GPa (Zhuravlev et al. 2010), whereas a PXRD study on $(Mg_{0.06}Fe_{0.94})O$ bracketed the cubic to rhombohedral transition between 13 and 24 GPa (Wicks et al. 2015). The rhombohedral distortion may also be associated with a magnetic transition at or near the structural transition pressure (Struzhkin et al. 2001; Jacobsen and Spetzler 2004; Kantor et al. 2004; Wicks et al. 2010).

Diffraction methods are generally used in compression experiments to probe the volume reduction of the crystallographic unit cell with pressure, and thus bulk compressibility, as well as any structural transitions that may occur. Pressure-volume relationships are frequently modeled with an equation of state, which results in an estimate of a material's isothermal bulk modulus, K_T, as well as its pressure derivative, K'_T. When constrained well by the measured data, these parameters can be used in the calculation of sound velocities and density profiles, and then compared to observed seismic data.

In a high-pressure apparatus such as a diamond-anvil cell, where sample dimensions are frequently limited to tens of micrometers, diffraction from powdered samples often suffers from poor grain statistics, has difficult-to-fit overlapping peaks, and the scattered intensity is significantly weaker than that of similarly sized single crystals. Combined, these effects tend to result in increased data scatter of compression curves measured from powdered samples compared with those from single crystals. Therefore, to more conclusively determine its compression behavior, here we expand on the previous study of ground, polycrystalline $(Mg_{0.22}Fe_{0.78})O$ by compressing and measuring the SXRD of single crystals drawn from the same batch of sample used in earlier work. Furthermore, we evaluate the influence of the pressure medium by running experiments in two different commonly used quasihydrostatic media: neon and helium. We complement the SXRD measurements with high-resolution time-domain synchrotron Mössbauer spectroscopy to tightly constrain the ferric iron concentration that, coupled with diffraction data, helps constrain the defect concentration.

EXPERIMENTAL PROCEDURES

We prepared two diamond-anvil cells (DAC) for high-pressure experiments. One cell was a standard Princeton-design symmetric DAC with a cubic boron nitride seat on the cylinder side and a tungsten carbide seat on the piston side. Standard modified brilliant-cut diamond anvils with flat 300 μm culets were used on both seats. The other DAC was a BX90 cell (Kantor et al. 2012) with symmetric Boehler-Almax-geometry seats (Boehler and De Hantsetters 2007) and diamonds with 250 μm beveled culets. Each cell's ~40 μm thick rhenium gasket was loaded with a nearly identical sample configuration that consisted of two or three <10 μm thick ruby sphere pressure calibrants and platelets of synthetic $(Mg_{0.22}Fe_{0.78})O$ magnesiowüstite, hereafter referred to as Mw78, <10 μm in thickness and ~20–30 μm in diameter. These small pieces were broken off from a larger single crystal. Additional details regarding the synthesis and characterization of this sample material may be found in previous publications (Jacobsen 2002; Mackwell et al. 2005). The prepared DACs were

subsequently gas-loaded with neon (symmetric DAC) or helium (BX90 DAC) pressure media at ~25 000 PSI using either the Caltech or COMPRES/GSECARS gas-loading system (Rivers et al. 2008), respectively (see supplementary information[1] for images of sample chambers at high pressure).

The ambient diffraction pattern of a portion of the magnesiowüstite sample was characterized at the 11.3.1 beamline of the Advanced Light Source at Lawrence Berkeley National Laboratory (λ = 0.6702 Å) (Fig. 1). Single-crystal diffraction measurements at high pressures were collected on each DAC sample configuration at the Advanced Photon Source at Argonne National Laboratory. The He-medium experiment was conducted at the PX^2 BM-C beamline (λ = 0.4340 Å) and the Ne-medium experiment at the ID-D beamline (λ = 0.3100 Å) of the GSECARS sector. We achieved maximum pressures of 55.5(3) and 53.3(1.5) GPa, respectively. Downstream X-ray opening angles of the loaded cells were determined to be 48° (Ne) and 60° (He). The number of measured diffraction peaks at each pressure point is determined by lattice-parameter lengths, X-ray energy, and opening angle of the diamond-anvil cell. After each pressure increase, the cell was allowed to rest for at least 20 min before collection of diffraction, minimizing pressure creep. Ruby spectra were obtained immediately after the diffraction patterns were collected for a given compression step. Several experiments using similar methods for the collection of single-crystal diffraction patterns at high pressure can be found in the recent literature, providing additional details on the procedure (Dera et al. 2013a; Finkelstein et al. 2014).

Experimental pressures were determined using the ruby scale of Dewaele et al. (2004). The uncertainty in pressure at each step was estimated as the standard deviation of the pressures measured for the different rubies in each sample chamber. Diffraction peaks were fit and lattice parameters refined in either the APEX 2 (ambient measurements) (Bruker 2012a) or the GSE_ADA/RSV (high-pressure measurements) (Dera et al. 2013b) software package. Unit cells were indexed based on an analysis of reciprocal lattice difference vectors within the RSV interface using the CELL_NOW (Bruker 2012b) program to (refer to discussion below and supplementary information[1] for example images of indexed reciprocal lattices and unique diffraction peaks used). After converting lattice parameters to unit-cell volumes, a third-order Birch-Murnaghan equation of state was fit to the pressure-volume data of each experimental run using the MINUTI software package (ver.2.0) (Sturhahn 2015a). The third-order Birch-Murnaghan equation of state takes the form:

$$P(V) = \frac{3K_{0T}}{2}\left[\left(\frac{V_0}{V}\right)^{\frac{7}{3}} - \left(\frac{V_0}{V}\right)^{\frac{5}{3}}\right]\left\{1 + \frac{3}{4}\left(K'_{0T} - 4\right)\left[\left(\frac{V_0}{V}\right)^{\frac{2}{3}} - 1\right]\right\}.$$

The parameters of pressure, unit-cell volume, zero-pressure unit-cell volume, and isothermal zero-pressure bulk modulus and its pressure derivative are represented by the symbols P, V, V_0, K_{0T}, and K'_{0T}, respectively. Using a new feature of MINUTI, we computed the covariance matrix of each of our equation of state fits as a function of pressure. The covariance matrices were used to calculate 68 and 95% confidence ellipses for our fit equation of state parameters, also as a function of pressure (Sturhahn 2015a); the reader is referred to Angel (2000) for more information on covariance matrices and confidence ellipses as they relate to equations of state as a function of pressure.

To complement our diffraction experiments and aid in the determination of the ferric content of our sample, we applied synchrotron Mössbauer spectroscopy (SMS) at APS Sector 3-ID-B in hybrid top-up mode. The measured single-crystalline platelet of Mw78 was ~110 μm thick, resulting in an effective thickness of about 10. The X-rays were focused to ~10 × 11 μm² (Zhang et al. 2015), and a high-resolution monochromator provided an energy bandwidth of 1 meV at the 14.4125 keV ^{57}Fe nuclear transition energy (Toellner 2000). The SMS spectrum was fit using the CONUSS software package (Sturhahn 2015b). With our use of APS hybrid mode, a time range of 35 to 860 ns became accessible for the SMS spectrum. This extended time range translates into a much improved energy resolution of about 1.1 Γ (Γ = 4.66 neV is the natural line width of the 14.4125 keV ^{57}Fe nuclear excited state) which compares to >2 Γ for conventional Mössbauer experiments using a radioactive source (Sturhahn 2001, Eq. 13 therein). At present, experiments using the hybrid mode require long data collection times due to limited useful X-ray intensity. Therefore, our SMS spectrum collected with the extended time range
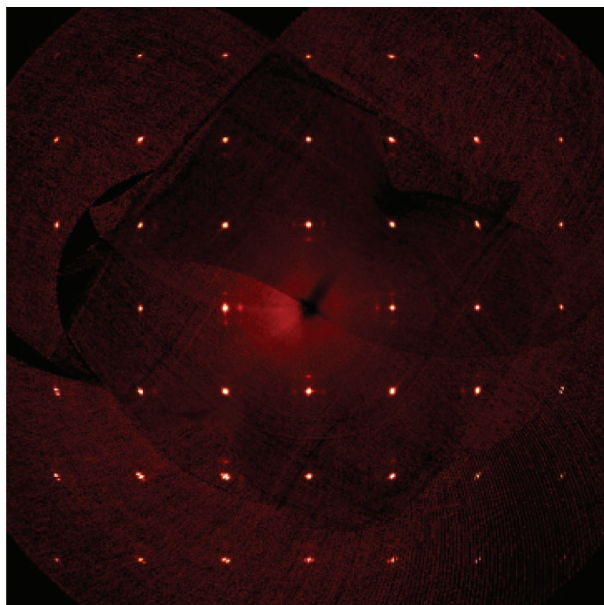
FIGURE 1. Pseudo-precession *hk*0 image of Mw78 diffraction at ambient conditions collected in air at ALS 11.3.1. Weak satellite peaks and diffuse scattering can be seen around the main Bragg reflections.

took about 20 h of beamtime. However, there is a clear advantage in taking SMS spectra in hybrid mode. Out of the various kinds of Mössbauer spectroscopy, this configuration has the best energy resolution to date, leading to markedly improved accuracy in the fit of potential minor sites and to finely resolved small differences in hyperfine parameters.

RESULTS AND DISCUSSION

Room pressure

At ambient conditions, the Mw78 crystal can be nominally indexed with a cubic unit cell (Table 1). However, upon closer examination of the diffraction peaks at long exposure times, faint, diffuse satellites are observed around the primary peaks, with their intensity significantly decreasing at high 2θ angles (Fig. 1). This additional scattering has been observed in several previous studies on the wüstite end-member (Hazen and Jeanloz 1984; Jacobsen et al. 2005), but has not previously been reported for (Mg,Fe)O solid solutions. The complex intensity distribution around the satellite peaks of wüstite has been interpreted as being directly related to an inhomogeneous paracrystalline structure that consists of regions of high defect-cluster density and regions of low defect-cluster density (Welberry and Christy 1997; Saines et al. 2013). As the observed scattering due to the defect structure is extremely weak, in this paper we use the Bragg peak positions alone to determine lattice parameter values, even though we recognize that they do not fully describe the sample's structure.

By fitting the SMS spectrum of our sample, we were able to quantify its ferric and ferrous components (Fig. 2). While the bulk (Mg,Fe)O structure is composed of octahedrally coordinated ferrous Fe, the defect structure is thought to be made of clusters of tetrahedrally coordinated ferric Fe. These two types of Fe can be readily distinguishable in an SMS spectrum, as the hyperfine fields (e.g., isomer shift, quadrupole splitting) are sensitive to

both oxidation state and coordination number.

Previously published SMS and conventional Mössbauer studies on (Mg,Fe)O and wüstite (e.g., Johnson 1969; Lin et al. 2006; McCammon et al. 1985; Solomatova et al. 2016) have used several different models to fit the complex observed spectra, ranging from a single doublet (Lin et al. 2006) to multiple doublets and singlets (McCammon and Price 1985). After investigating these and similar models, we concluded that our spectrum required a model with four Fe sites to achieve an optimal and physically meaningful fit. These four sites consist of three doublets and one singlet. The SMS spectrum was collected without an external reference standard, such as a stainless steel foil, which would permit determination of all isomer shifts. However, by fixing three of the doublets to an isomer shift of 1.0 mm/s (a value that is reasonable for an octahedrally coordinated ferrous Fe site), we determine the relative isomer shift of the fourth site. Combined, the three doublet sites correspond to ~94% of the Fe sites, and have quadrupole splitting values ranging from 0.6 to 1.3 mm/s (Table 1, Fig. 2). In light of this information, we assign the three doublets to high-spin ferrous sites. The singlet, on the other hand, exhibited an isomer shift ~0.95 mm/s lower than the other sites, which is consistent only with tetrahedrally coordinated high-spin ferric Fe (Dyar et al. 2006). This interpretation is distinct from select Mössbauer studies on wüstite, where the singlet site was interpreted as a component of the metallic iron sextet (McCammon and Price 1985). Renormalizing the measured Mw78 sample composition to take into account the vacancies necessitated by the ferric Fe content results in a composition of $(Mg_{0.215}Fe^{2+}_{0.716}$ $Fe^{3+}_{0.046}\square_{0.023})O$ if ferric and ferrous Fe are separated in the chemical formula, and $(Mg_{0.215}Fe_{0.762}\square_{0.023})O$ if not distinguished.

High pressure

Phase stability. At low pressures, the Mw78 crystal in neon has a diffraction pattern that can be indexed with the expected cubic unit cell (Fig. 1). At high pressures, the diffraction peak positions are no longer compatible with this unit-cell geometry, and a lower-symmetry cell is required. We do not see evidence for twinning in the high-pressure phase. With the obtained coverage of reciprocal space, a hexagonal unit cell is sufficient for fitting the observed unit-cell distortion. Deviations from cubic symmetry can be quantified by monitoring the *c/a* lattice parameter ratio. Figure 3a (bottom) shows the pressure dependence of the *c/a* ratio, which has a value of $\sqrt{6} \approx 2.45$ for a cubic material. A Mw78 crystal in neon remains cubic until ~20 GPa, above which it becomes increasingly hexagonal (as observed by analy-

TABLE 1. Mw78 room-pressure best-fit hyperfine parameters

| Site	Coordination environment	Weight fraction (%)	IS (mm/s)	QS (mm/s)	FWHM (mm/s)
Fe^{2+}_A	Octahedral	69.7(1.0)	1.0[b]	0.592(3)	0.1319(14)[c]
Fe^{2+}_B	Octahedral	17.3(1.0)	1.0[b]	0.913(5)	0.1319(14)[c]
Fe^{2+}_C	Octahedral	7[a]	1.0[b]	1.307(7)	0.1319(14)[c]
Fe^{3+}_D	Tetrahedral	6[a]	0.044(10)	0	0.427(12)

Notes: Thickness = 137.6(1.3) μm, Lamb Mössbauer factor = 0.75. IS = isomer shift, QS = quadrupole splitting, FWHM = full-width at half maximum, reduced chi-squared = 1.02(7).
[a] These site fractions were manually varied to optimize the fit.
[b] The isomer shift for these sites was fixed so that the relative isomer shift for the ferric Fe site could be reported.
[c] The widths of the doublet sites were constrained to be identical to each other.
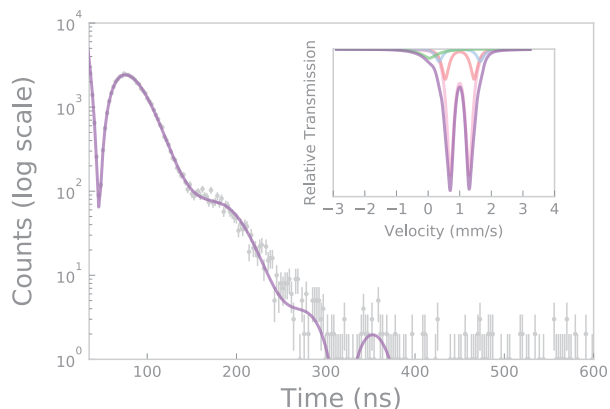
FIGURE 2. Synchrotron Mössbauer spectrum of the Mw78 single crystal at room pressure. The raw data and associated 1σ error bars are shown as light-gray markers, and the best-fit model is shown as a purple line. The inset shows the calculated energy spectrum using the best-fit parameters from the measured time spectrum and the contributions to the fit from each individual site (pink, red, blue, and green correspond to the Fe_A^{2+}, Fe_B^{2+}, Fe_C^{2+}, and Fe_D^{3+} sites described in Table 1). In this calculation the absolute isomer shift is arbitrary, and only the relative isomer shift is meaningful.

sis of the reciprocal lattice difference vectors, see Fig. 3b). In contrast, a Mw78 crystal in the helium pressure medium gives a c/a ratio near 2.45 over the whole pressure range, indicating that the unit cell remains metrically cubic up to the maximum pressure of our study. Lattice parameter values refined in both the cubic and hexagonal settings are provided in Table[1] 2.

Previous high-pressure studies on $(Mg_{0.22}Fe_{0.78})O$ and $(Mg_{0.06}Fe_{0.94})O$ in neon reported rhombohedral transitions around 20–40 and 13–24 GPa, respectively (Zhuravlev et al. 2010). These results are compatible with our result on Mw78 in neon. High-pressure studies of helium-loaded wüstite single crystals

(Shu et al. 1998; Jacobsen et al. 2005) reported fourfold non-merohedral twinning inherent to the mechanism of a rhombo-hedral transition in wüstite. Our single-crystal diffraction study on Mw78 in helium shows no evidence for a lower symmetry distortion up to 55 GPa. The addition of MgO to wüstite appears to extend the stability field of the cubic phase.

Since ruby spheres were placed in several locations inside the sample chamber of each DAC (refer to supplementary[1] figures for pictures), we were able to use the standard deviation of the calibrated ruby pressures as a proxy for nonhydrostatic-ity experienced by the sample. As seen in Figure 3a (top), this quantity remains near zero for the helium-loaded sample cham-ber, but rapidly increases in the neon-loaded sample chamber above ~20 GPa. The nonhydrostaticity proxy shows the exact same pressure dependence as the hexagonal distortion of Mw78 described earlier. Previous work also investigated the quasi-hydrostatic pressure limits of helium and neon media using the ruby standard deviation method up to ~40 and ~50 GPa, respectively (Klotz et al. 2009). Their results suggest that while nonhydrostaticity in a neon medium increases rapidly above ~15 GPa, nonhydrostaticity in a helium medium increases gradu-ally above ~23 GPa.

Equations of state. Figure 4 shows compression curves for single-crystalline Mw78 in helium (indexed as cubic) and neon (indexed as cubic and hexagonal), and for powdered $(Mg_{0.22}Fe_{0.78})O$ in neon (Zhuravlev et al. 2010) (indexed as cubic). There is a discernible difference between the Mw78 in neon and in helium, as the Mw78 sample in helium is more compressible than those in neon. The compression curves are smooth for each phase and are each well described by a third-order Birch-Murnaghan equation of state. Our optimiza-tion procedure using the MINUTI software (Sturhahn 2015a) incorporated the measured ambient unit-cell volume from ALS 11.3.1 of 78.94 ± 0.1 Å^3 for our single-crystal cubic-indexed measurements as a prior on V_0. For the crystal in helium, the
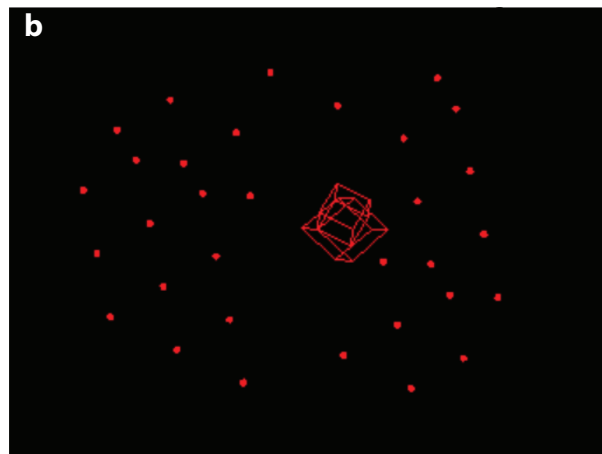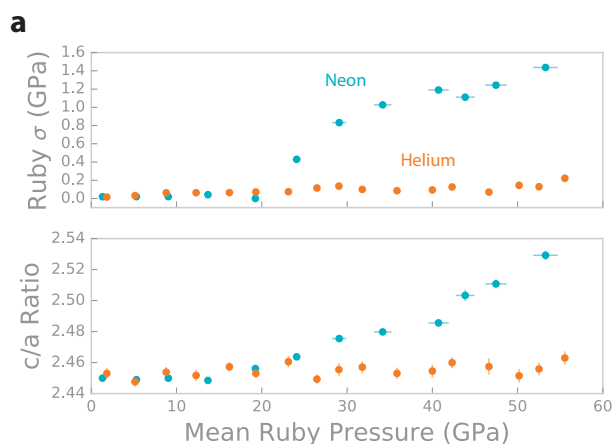
FIGURE 3. (a, top) Ruby standard deviation as a function of mean ruby pressure for both helium- (orange circles) and neon-loaded (cyan circles) diamond-anvil cells. (**a, bottom**) c/a ratio as a function of mean ruby pressure for both helium- (orange circles) and neon-loaded (cyan circles) diamond-anvil cells. Uncertainty in pressure is represented as one ruby standard deviation. Error bars are not given for the ruby standard deviation, and, when not visible, other error bars are smaller than the symbol size. Error in c/a ratio represents a 1σ uncertainty that has been propagated from lattice parameter fits. When not visible, error bars are smaller than the symbol size. (**b**) The reciprocal lattice of the single-crystal in neon at 53.3 GPa. Red vectors outline the hexagonal unit cell and its relationship to a pseudo-cubic unit cell.
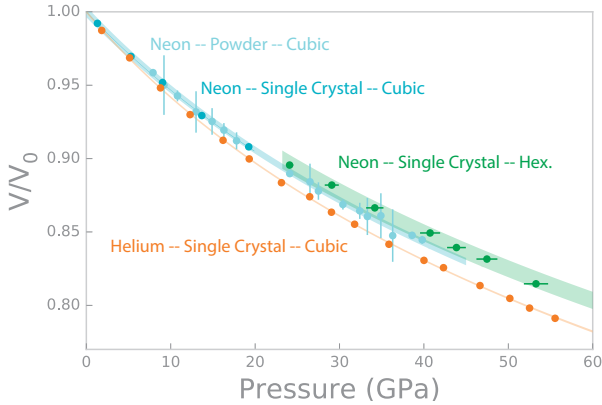
FIGURE 4. Normalized unit-cell volumes of Mw78 and equations of state fit using MINUTI (Sturhahn 2015a). Orange, dark cyan/green, and light cyan symbols correspond to diffraction from a single crystal of Mw78 in helium (this study, indexed using a cubic unit cell), a single crystal of Mw78 in neon (this study, indexed using a cubic unit cell below and a hexagonal unit cell above 20 GPa), and powdered $(Mg_{0.22}Fe_{0.78})O$ in neon (Zhuravlev et al. 2010), respectively. Circles represent measured unit-cell volumes normalized by the zero-pressure unit-cell volume resulting from a fit by a third-order Birch-Murnaghan equation of state. Uncertainty in pressure is represented as one ruby standard deviation. Shaded regions represent the fit third-order Birch-Murnaghan equations of state with 1σ fitting errors. Where not visible, vertical error bars on individual data points are smaller than the symbol size.

other parameters, K_{0T} and K'_{0T}, were allowed to vary freely. For the crystal in neon, due to the limited number of data points in respective phase regions, a strong prior of ±0.1 was put on K'_{0T} for both the cubic (1.3–19.2 GPa) and hexagonal (24.1–53.3 GPa) phases. The best fits to the data were achieved with V_0, K_{0T}, and K'_{0T} values of 78.742(14) Å^3, 163.0(1.0) GPa, and 4.02(10) for the cubic-indexed single-crystal Mw78 in neon and 78.87(6) Å^3, 148(3) GPa, and 4.09(12) for the cubic-indexed single crystal Mw78 in helium, V_0, K_{0T}, and K'_{0T} values of 78.5(2) Å^3, 166(5) GPa, and 4.01(10) for the cubic-indexed powdered Mw78 in neon, and V_0, K_{0T}, and K'_{0T} values of 58.7(4) Å^3, 176.8(1.1) GPa, and 4.00(10) for the hexagonal-indexed single-crystal Mw78

in neon. These fits are plotted in Figure 4. While both single-crystal cubic compression curves have similar K'_{0T} values (~4), the cubic phase of the sample in neon exhibits a significantly higher value for K_{0T} compared with the sample in helium. This corresponds to higher values of V/V_0 for the sample in neon at pressures above ~5 GPa (Fig. 4), and is consistent with Mw78 being very sensitive to nonhydrostaticity, as neon crystallizes at ~4.8 GPa (Klotz et al. 2009). While in our diffraction experiments we cannot confidently resolve a hexagonal distortion in Mw78 until above ~20 GPa, the unit-cell volume appears to be affected by neon crystallization below ~20 GPa.

To provide context for our results, we re-evaluated equations of state for data on several (Mg,Fe)O compositions using MINUTI for direct comparison with our study (Table 3). Pressure-volume data were sourced from single-crystal diffraction studies by Jacobsen (2002) and Jacobsen et al. (2005, 2008) and a powder diffraction study by Zhuravlev et al. (2010). Since Zhuravlev et al. (2010) did not collect data near zero pressure, we applied a prior of 4.0 ± 0.1 on K'_{0T} in the equation of state fit. The Jacobsen et al. (2005) data on cubic-structured $Fe_{0.93}O$ covered a limited pressure range, and therefore we also applied a prior of 4.0 ± 0.1 on K'_{0T}. This value is consistent with the given $Fe_{0.93}O$ data, as well as with the Mw78 single-crystal diffraction measurements in helium. All other parameters remained unconstrained during fitting.

All examined (Mg,Fe)O data sets are fit well by a third-order Birch-Murnaghan equation of state. We show the 68 and 95% confidence ellipses (joint probability) for each pair of equation of state fit parameters as a function of pressure in Figure 5. Confidence ellipses, which are derived from the fit-parameter covariance matrix, visualize magnitude and sign of parameter correlations and provide insight into the acceptable parameter space. The primary correlation in a third-order Birch-Murnaghan equation of state fit is between K_T and K'_T. As discussed in Angel (2000), this parameter correlation is initially negative but continuously changes to a positive correlation with pressure. Consequently, for every equation of state fit, there is some pressure where K_T and K'_T are uncorrelated and uncertainties of the fit parameters are lowest. This pressure primarily depends on the pressure range of a data set but is also sensitive to the data

TABLE 3. Selected 300 K (Mg,Fe)O equation of state fit parameters

Work[d]	Composition	Medium	Technique	P range (GPa)	V_0 (Å^3)	K_{0T} (GPa)	K'_{0T}
Jacobsen et al. (2005)	$Fe_{0.93}O$	Helium	SXRD	0–22.8	79.41(4)	145.7(1.2)	3.99(6)[b]
				Published Fit:	*79.41(4)*	*146(2)*	*4.0 (fixed)*
This Study (cubic)	$(Mg_{0.22}Fe_{0.78})O$	Helium	SXRD	1.8–55.5	78.87(6)[a]	148(3)	4.09(12)
This Study (cubic)	$(Mg_{0.22}Fe_{0.78})O$	Neon	SXRD	1.3–19.2	78.742(14)[a]	163.0(1.0)	4.02(10)[b]
This Study (hex.)	$(Mg_{0.22}Fe_{0.78})O$	Neon	SXRD	24.1–53.3	58.7(4)	176.8(1.1)	4.00(10)[b]
Zhuravlev et al. (2010)	$(Mg_{0.22}Fe_{0.78})O$	Neon	PXRD	7.9–39.8	78.5(2)	166(5)	4.01(10)[b]
				Published Fit:	*78.49(21)*	*166(5)*	*4.0 (fixed)*
Jacobsen et al. (2002)	$(Mg_{0.25}Fe_{0.75})O$	4:1 Meth-Eth	SXRD	0–7.2	78.082(3)	151.3(7)	5.6(2)
				Published Fit:	*78.082(3)*	*151.3(6)*	*5.55(19)*
Jacobsen et al. (2002)	$(Mg_{0.44}Fe_{0.56})O$	4:1 Meth-Eth	SXRD	0–8.9	77.457(4)	155.2(8)	5.7(3)
				Published Fit:	*77.453(4)*	*155.8(9)*	*5.5(2)*
Jacobsen et al. (2002)	$(Mg_{0.73}Fe_{0.27})O$	4:1 Meth-Eth	SXRD	0–9.3	76.336(3)	158.4(5)	5.48(11)
				Published Fit:	*76.336(3)*	*158.4(4)*	*5.49(11)*
Jacobsen et al. (2005)	$(Mg_{0.73}Fe_{0.27})O$	Helium	SXRD	0–51.1	77.30(4)	154.8(1.9)	3.97(10)
				Published Fit:	*76.30(9)*	*154(3)*	*4.0(1)*
Jacobsen et al. (2008)	MgO	Helium	SXRD	0–118.1	74.707(5)	160.08(14)	4.030(4)
				Published Fit:	*74.697(6)*	*160.2[c]*	*4.03[c]*

[a] Prior of $V_0 = 78.94 \pm 0.1$ Å^3 used during equation of state fit. [b] Prior of $K'_{0T} = 4.0 \pm 0.1$ used during equation of state fit. [c] From Zha et al. (2000) MgO primary pressure scale.
[d] If symmetry is not noted, the data sets represent cubic forms of (Mg,Fe)O.
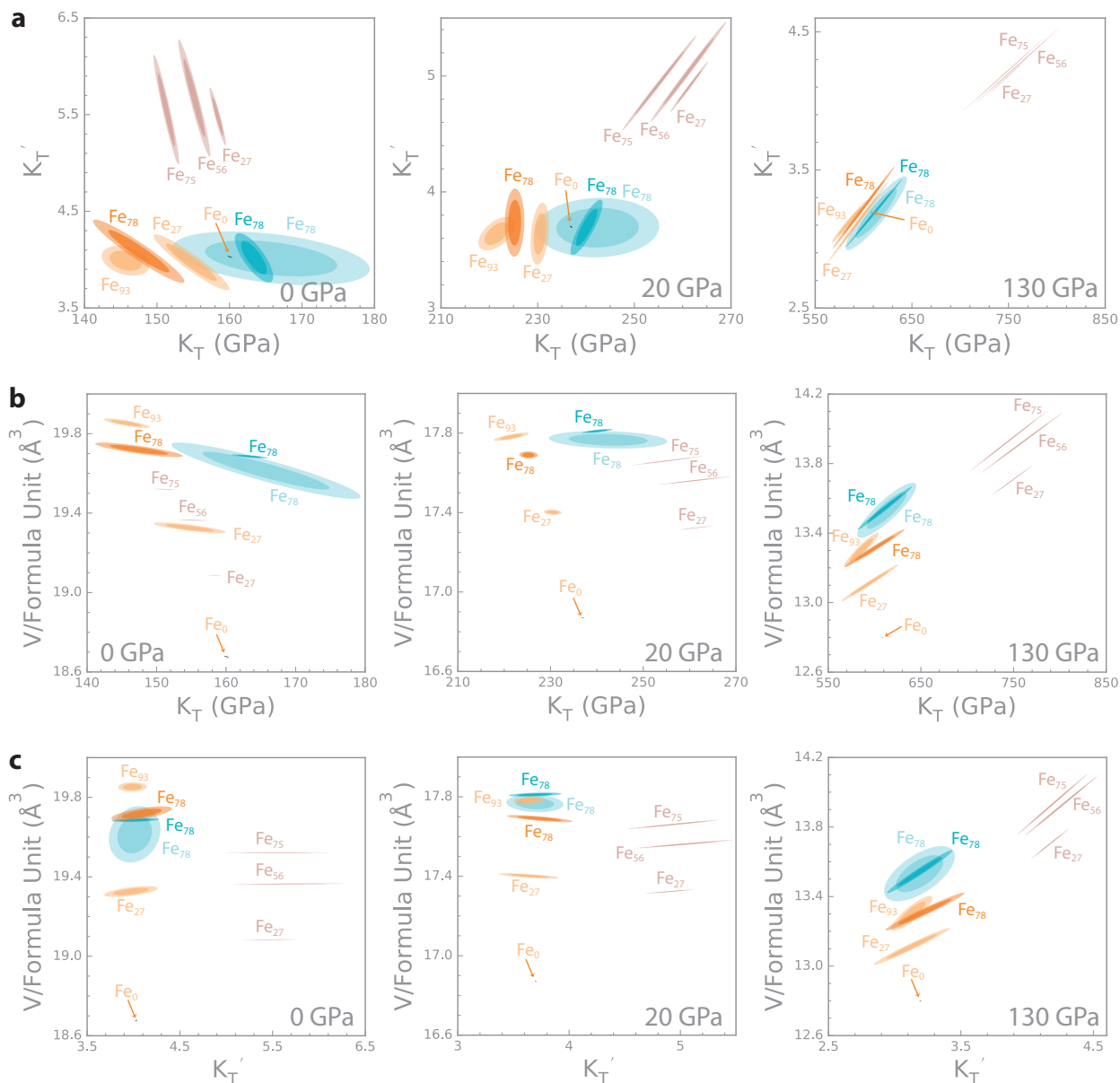
FIGURE 5. (a) Confidence ellipses of K_T and K_T' at 68 and 95% levels for several (Mg,Fe)O compositions at 0, 20, and 130 GPa. Orange, cyan, and brown ellipses represent diffraction measurements in helium, neon, and 4:1 methanol-ethanol pressure media (Jacobsen 2002; Jacobsen et al. 2005, 2008; Zhuravlev et al. 2010), respectively. Darker ellipses correspond to samples from this study (the ellipses corresponding to the sample in Ne are derived from the covariance matrix of the equation of state fit to the low-pressure cubic-indexed data points). **(b)** Confidence ellipses of V and K_T. **(c)** Confidence ellipses of V and K_T'.

distribution and uncertainties. In our fits, the pressure where K_T and K_T' are uncorrelated is between 5 and 20 GPa, depending on the data set. Above this pressure, K_T and K_T' are positively correlated, and their uncertainties increase rapidly for pressures outside of the measured range.

In Figure 6, we present F-f plots for all our (Mg,Fe)O equation of state fits, with separate subplots for samples compressed in helium, neon, and 4:1 methanol-ethanol pressure media. F-f plots show normalized pressure (F) as a function of Eulerian strain (f), and can be useful for estimating K_{0T} and K_{0T}' parameter values of

a third-order Birch-Murnaghan equation of state. In an F-f plot, if a straight line can be fit to a given data set, its F-axis intercept corresponds to the approximate value of K_{0T}. A positive or negative slope of the line indicates a value of K_{0T}' that is either greater than or less than 4, respectively. A slope of zero means that K_{0T}' equals 4 which effectively reduces the order and represents a second-order Birch-Murnaghan equation of state. If a straight line does not properly model the F-f plot a higher-order equation of state is required to fit the pressure-volume data. Specific results for each pressure medium will be discussed below.
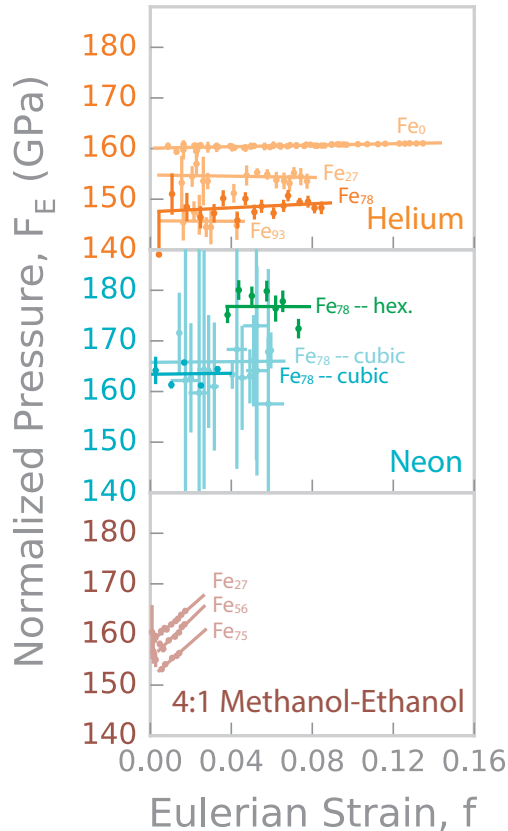
FIGURE 6. Plots of normalized pressure (*F*) as a function of Eulerian strain (*f*) corresponding to compression data (filled circles with error bars) and equation of state fits (solid lines) for various (Mg,Fe)O compositions (Jacobsen 2002; Jacobsen et al. 2005, 2008; Zhuravlev et al. 2010). (**top**) Single-crystal studies in a helium pressure medium. (**middle**) Single-crystal and powder studies in a neon pressure medium. Dark green and dark cyan data points are from the same sample, and represent fits to the portions of the data that can be indexed using cubic and hexagonal unit cells, respectively. For the data from the samples in a neon pressure medium, a strong prior was placed on K'_{0T}, causing it to stay near a value of 4.0 ± 0.1 during fitting. (**bottom**) Single-crystal studies in a 4:1 methanol-ethanol pressure medium. Darker symbols/lines correspond to data collected for this study and lighter symbols/lines correspond to previous studies. The error bars in *F* and *f* correspond to 1σ uncertainties, and when not visible, are smaller than the symbol size (see Angel 2000 for details on *F-f* plot error bar calculations). Uncertainties are not given for the lines corresponding to the equation of state fits.

The *F-f* plots of the samples in both helium and neon media show near-zero slopes, which indicates a compositionally independent K'_{0T} value of about 4 that is consistent with observations of low-Fe compositions with FeO ≤ 17 mol% from ultrasonic and Brillouin measurements. There have been no high-pressure reports of both the compressional and shear velocities to compute the bulk modulus, required for constraining a pressure derivative, for samples with greater iron content. The positive *F-f* slopes in the samples compressed in 4:1 methanol-ethanol require a different explanation, as this pressure medium is believed to remain hydrostatic to ~10 GPa (Klotz et al. 2009). Jacobsen et al. (2005) speculated that they may be related to the limited

maximum compression of the samples or to differences between the quartz pressure scale and others that are used more commonly (e.g., ruby fluorescence).

The *F*-intercepts on the *F-f* plots suggest a decrease in K_{0T} with increasing iron content for samples compressed in helium and 4:1 methanol-ethanol, the pressure media in which the compression of multiple (Mg,Fe)O compositions has been measured. These trends, with slopes of about –0.15 GPa/mol%, are shown in Figure 7. Even though the trends have similar slopes, the methanol-ethanol trend is offset in K_{0T} by about 3 GPa. It should be noted that the methanol-ethanol K_{0T} values are not necessarily expected to be similar to those in other pressure media, as these data sets cannot be fit with a K'_{0T} near 4, and require a significantly higher value of ~5.5 (see Table 3). The best-fit K_{0T} values of 163.0(1.0) and 166(5) GPa for the cubic-indexed Mw78 single crystal and powder in neon, respectively, are consistent with each other. They show essentially the same result of $K_{0T} = 160(2)$ GPa and $K'_{0T} = 4.12(14)$ that was reported for (Mg,Fe)O powder with 48 mol% FeO in neon using a spin-crossover equation of state (Solomatova et al. 2016).

Compositional dependence of the bulk modulus

Values for K_{0T} obtained from equation of state fits can also be compared to results using other methods such as Brillouin spectroscopy and ultrasonic interferometry, which determine sound velocities rather than density. Sound velocities and density are then combined to calculate the adiabatic bulk modulus K_S, which is related to K_T via $K_S = K_T (1 + \alpha\gamma T)$, where α is the volumetric thermal expansion coefficient, γ is the Grüneisen parameter, and *T* is temperature (in our case, 298 K). Lack of sufficient data for the compositional dependence of αγ in the (Mg,Fe)O system makes it unclear what values should be used, and therefore for
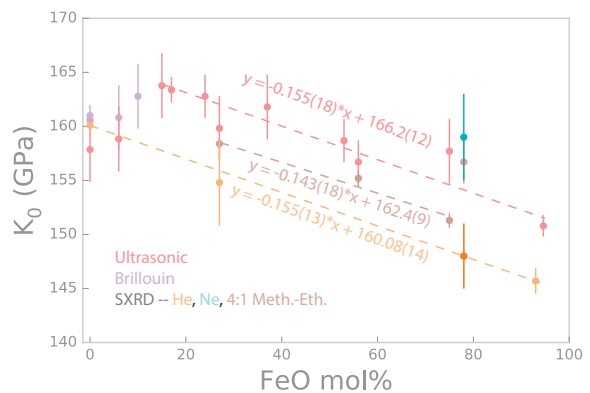
FIGURE 7. K_{0T} (diffraction) and K_{0S} (ultrasonic, Brillouin) compositional trends for (Mg,Fe)O solid solutions from single-crystal studies. Ultrasonic and Brillouin studies are represented by red and purple symbols, respectively. Single-crystal diffraction studies in helium, neon, and 4:1 methanol-ethanol pressure media are represented by orange, cyan, and brown symbols, respectively. The dashed lines show weighted linear least-square fits to the data. In the equations that correspond to the best-fit lines, *x* is the FeO mol% and *y* is either K_{0T} (diffraction) or K_{0S} (ultrasonic, Brillouin) in units of GPa. Compositional error bars are smaller than the symbol size and K_0 error bars are either 1σ uncertainties from equation of state fitting (diffraction) or those reported in the literature (Brillouin, ultrasonic).

Brillouin and ultrasonic studies we are plotting K_{0S}.

As reported previously by Jacobsen et al. (2002), K_{0S} trends differently for solid solutions containing low and high Fe content. Crystals with FeO mol% up to ~15% show an increasing K_{0S} with increasing iron content, albeit with small-number statistics, while those with higher FeO mol% show the opposite effect. This is in subtle contrast to equation of state fits to pressure-volume data from diffraction, which support a linear decrease in K_{0T} from MgO to $Fe_{1-x}O$. It should be noted that this trend is observed for single crystals that likely have an increasing amount of ferric iron toward the $Fe_{1-x}O$ end-member (this study, Jacobsen et al. 2002). Additional work is needed to reconcile this discrepancy, with a potential focus on the differential sensitivity of diffraction, ultrasonic, and Brillouin measurements to small proportions of a defect structure.

IMPLICATIONS

Pressure at the CMB is well established to be 135.8 GPa from the preliminary reference Earth model (PREM) (Dziewonski and Anderson 1981), however, the temperature at the CMB and the temperature profile near the CMB are less agreed upon. Candidate geotherms from van der Hilst et al. (2007) and Zhang et al. (2016) suggest that the upper bound for the core-mantle boundary temperature is ~4000 K, but the addition of minor amounts of light elements will likely depress this value. To compute geophysically relevant parameters of crystalline Mw78 at the CMB, we assume a CMB temperature of 3800 K (Zhang and Fei 2008; Fischer and Campbell 2010; Wicks et al. 2015; Kato et al. 2016) and thermal parameters of Debye temperature = 426 K, γ_0 = 1.72(8), and q = 0.5, as reported by Wicks et al. (2015) for $(Mg_{0.06}Fe_{0.94})O$, a composition similar to that explored in the current study. Extrapolating to the CMB pressure of 135.8 GPa at 300 K using the V_0, K_{0T}, and K'_{0T} parameters obtained from our single-crystal experiments in neon and helium (Table 3), we obtain a density of 8.03(3) g/cm³ for the sample in neon (using the equation of state parameters from the cubic-indexed data set) and 8.17(3) g/cm³ for the sample in helium. The ~2% density difference between these two calculations is about a factor of five higher than the uncertainty in density for the individual single-crystal equation of state studies presented here. This illustrates the benefits of using an equation of state from high-quality measurements. Applying thermal considerations to compute the density at 3800 K at the same pressure results in a density of 7.51 g/cm³ using the equation of state of the sample in neon and 7.63 g/cm³ for the sample in helium.

To place the value for density computed from our study using a helium pressure medium in the context of the 1D Earth model PREM, Mw78 is about 37% more dense than the average mantle at the CMB. On the core side of the CMB, Mw78 is about 23% less dense than the outer core. If magnesiowüstite with a similar composition to our sample existed above the core-mantle boundary, it would form morphologies explored in work by Bower et al. (2011) that depend on a small volume fraction mixed with silicates. It has recently been suggested that giant impacts over Earth's history could have resulted in the temperature-dependent dissolution of small amounts of Mg in the outer core, which then could have precipitated and floated to the core-mantle boundary as the core cools, helping to drive the geodynamo over billions of years (O'Rourke and Stevenson 2016). The precipitated Mg could react either with lower mantle material or any oxygen present as a light element in the outer core, to form MgO (Badro et al. 2016) or (Mg,Fe)O. As indicated by the density deficit of $(Mg_{0.22}Fe_{0.78})O$ compared with PREM, this material could be emplaced on the core-side of the core-mantle boundary, potentially percolate or diffuse into the lower mantle, and then stabilize at the base of the mantle.

To date, only a select number of (Mg,Fe)O compositions have been investigated using single-crystal diffraction at high pressure, and few Brillouin and ultrasonic studies exist with which to compare the results. In this paper, we provided constraints on the elastic behavior of Mw78 in helium and neon pressure media. From the significant differences of the corresponding compression behavior, we conclude that nonhydrostaticity has a strong influence on the appearance of distortions away from cubic symmetry in iron-rich (Mg,Fe)O compositions. In addition, the derived equations of state are clearly different, in particular at the high pressures relevant to lower mantle conditions. The study of single crystals in a helium pressure medium presents a valuable baseline upon which future studies can build, for example, by extending the pressure range and elevating the temperature.

REFERENCES CITED

Angel, R.J. (2000) Equations of state. Reviews in Mineralogy and Geochemistry, 41, 35–59.
Badro, J., Siebert, J., and Nimmo, F. (2016) An early geodynamo driven by exsolution of mantle components from Earth's core. Nature, 536, 326–328.
Boehler, R., and De Hantsetters, K. (2007) New anvil designs in diamond-cells. High Pressure Research, 24, 391–396.
Bower, D.J., Wicks, J.K., Gurnis, M., and Jackson, J.M. (2011) A geodynamic and mineral physics model of a solid-state ultralow-velocity zone. Earth and Planetary Science Letters, 303, 193–202.
Bruker (2012a) APEX2. Bruker AXS Inc., Madison, Wisconsin, U.S.A.
——— (2012b) CELL_NOW. Bruker AXS Inc., Madison, Wisconsin, U.S.A.
Dera, P., Finkelstein, G.J., Duffy, T.S., Downs, R.T., Meng, Y., Prakapenka, V., and Tkachev, S. (2013a) Metastable high-pressure transformations of orthoferrosilite Fs82. Physics of the Earth and Planetary Interiors, 221, 15–21.
Dera, P., Zhuravlev, K., Prakapenka, V., Rivers, M.L., Finkelstein, G.J., Grubor-Urosevic, O., Tschauner, O., Clark, S.M., and Downs, R.T. (2013b) High pressure single-crystal micro X-ray diffraction analysis with GSE_ADA/RSV software. High Pressure Research, 33, 466–484.
Dewaele, A., Loubeyre, P., and Mezouar, M. (2004) Equations of state of six metals above 94 GPa. Physical Review B, 70, 094112.
Dyar, M.D., Agresti, D.G., Schaefer, M.W., Grant, C.A., and Sklute, E.C. (2006) Mössbauer spectroscopy of Earth and planetary materials. Annual Review of Earth and Planetary Sciences, 34, 83–125.
Dziewonski, A.M., and Anderson, D.L. (1981) Preliminary reference Earth model. Physics of the Earth and Planetary Interiors, 25, 297–356.
Fei, Y., Wang, Y., and Finger, L.W. (1996) Maximum solubility of FeO in (Mg, Fe)SiO₃-perovskite as a function of temperature at 26 GPa: Implication for FeO content in the lower mantle. Journal of Geophysical Research, 101, 11525–11530.
Finkelstein, G.J., Dera, P.K., Jahn, S., Oganov, A.R., Holl, C.M., Meng, Y., and Duffy, T.S. (2014) Phase transitions and equation of state of forsterite to 90 GPa from single-crystal X-ray diffraction and molecular modeling. American Mineralogist, 99, 35–43.
Fischer, R.A., and Campbell, A.J. (2010) High-pressure melting of wüstite. American Mineralogist, 95, 1473–1477.

Hazen, R.M., and Jeanloz, R. (1984) Wüstite (Fe$_{1-x}$O): A review of its defect structure and physical properties. Reviews of Geophysics, 22, 37–46.

Irifune, T. (1994) Absence of an aluminous phase in the upper part of the Earth's lower mantle. Nature, 370, 131–113.

Jacobsen, S.D. (2002) Structure and elasticity of single-crystal (Mg,Fe)O and a new method of generating shear waves for gigahertz ultrasonic interferometry. Journal of Geophysical Research, 107, 2037.

Jacobsen, S.D., and Spetzler, H. (2004) Shear waves in the diamond-anvil cell reveal pressure-induced instability in (Mg,Fe)O. Proceedings of the National Academy of Sciences, 101, 5867–5871.

Jacobsen, S.D., Lin, J.-F., Angel, R.J., Shen, G., Prakapenka, V.B., Dera, P., Mao, H.-K., and Hemley, R.J. (2005) Single-crystal synchrotron X-ray diffraction study of wüstite and magnesiowüstite at lower-mantle pressures. Journal of Synchrotron Radiation, 12, 577–583.

Jacobsen, S.D., Holl, C.M., Adams, K.A., Fischer, R.A., Martin, E.S., Bina, C.R., Lin, J.F., Prakapenka, V.B., Kubo, A., and Dera, P. (2008) Compression of single-crystal magnesium oxide to 118 GPa and a ruby pressure gauge for helium pressure media. American Mineralogist, 93, 1823–1828.

Johnson, D.P. (1969) Mössbauer study of the local environments of ^{57}Fe in FeO. Solid State Communications, 7, 1785–1788.

Kantor, I.Y., McCammon, C.A., and Dubrovinsky, L.S. (2004) Mössbauer spectroscopic study of pressure-induced magnetisation in wüstite (FeO). Journal of Alloys and Compounds, 376, 5–8.

Kantor, I., Prakapenka, V., Kantor, A., Dera, P., Kurnosov, A., Sinogeikin, S., Dubrovinskaia, N., and Dubrovinsky, L. (2012) BX90: A new diamond anvil cell design for X-ray diffraction and optical measurements. Review of Scientific Instruments, 83, 125102.

Kato, C., Hirose, K., Nomura, R., Ballmer, M.D., Miyake, A., and Ohishi, Y. (2016) Melting in the FeO-SiO$_2$ system to deep lower-mantle pressures: Implications for subducted banded iron formations. Earth and Planetary Science Letters, 440, 56–61.

Klotz, S., Chervin, J.-C., Munsch, P., and Le Marchand, G. (2009) Hydrostatic limits of 11 pressure transmitting media. Journal of Physics D: Applied Physics, 42, 075413.

Lin, J.-F., Gavriliuk, A.G., Struzhkin, V.V., Jacobsen, S.D., Sturhahn, W., Hu, M.Y., Chow, P., and Yoo, C.-S. (2006) Pressure-induced electronic spin transition of iron in magnesiowüstite-(Mg,Fe)O. Physical Review B, 73, 113107.

Lin, J.F., Vanko, G., Jacobsen, S.D., Iota, V., Struzhkin, V.V., Prakapenka, V.B., Kuznetsov, A., and Yoo, C.S. (2007) Spin transition zone in Earth's lower mantle. Science, 317, 1740–1743.

Mackwell, S., Bystricky, M., and Sproni, C. (2005) Fe–Mg interdiffusion in (Mg,Fe)O. Physics and Chemistry of Minerals, 32, 418–425.

Manga, M., and Jeanloz, R. (1996) Implications of a metal-bearing chemical boundary layer in D″ for mantle dynamics. Geophysical Research Letters, 23, 3091–3094.

Mao, H. (1997) Multivariable dependence of Fe-Mg partitioning in the lower mantle. Science, 278, 2098–2100.

Mao, W.L., Mao, H.-K., Sturhahn, W., Zhao, J., Prakapenka, V.B., Meng, Y., Shu, J., Fei, Y., and Hemley, R.J. (2006) Iron-rich post-perovskite and the origin of ultralow-velocity zones. Science, 312, 564–565.

Mao, Z., Lin, J.-F., Liu, J., and Prakapenka, V.B. (2011) Thermal equation of state of lower-mantle ferropericlase across the spin crossover. Geophysical Research Letters, 38, L23308.

McCammon, C.A., and Price, D.C. (1985) Mössbauer spectra of Fe$_x$O (x>0.95). Physics and Chemistry of Minerals, 11, 250–254.

Ohta, K., Fujino, K., Kuwayama, Y., Kondo, T., Shimizu, K., and Ohishi, Y. (2014) Highly conductive iron-rich (Mg,Fe)O magnesiowüstite and its stability in the Earth's lower mantle. Journal of Geophysical Research (Solid Earth), 119, 4656–4665.

O'Rourke, J.G., and Stevenson, D.J. (2016) Powering Earth's dynamo with magnesium precipitation from the core. Nature, 529, 387–389.

Rivers, M., Prakapenka, V.B., Kubo, A., Pullins, C., Holl, C.M., and Jacobsen, S.D. (2008) The COMPRES/GSECARS gas-loading system for diamond anvil cells at the Advanced Photon Source. High Pressure Research, 28, 273–292.

Rost, S., Garnero, E.J., and Williams, Q. (2006) Fine-scale ultralow-velocity zone structure from high-frequency seismic array data. Journal of Geophysical Research, 111, B09310.

Saines, P.J., Tucker, M.G., Keen, D.A., Cheetham, A.K., and Goodwin, A.L. (2013) Coupling of the local defect and magnetic structure of wüstite Fe$_{1-x}$O. Physical Review B, 88, 134418.

Shu, J., Mao, H., Hu, J., and Fei, Y. (1998) Single-crystal X-ray diffraction of wüstite to 30 GPa hydrostatic pressure. Neues Jahrbuch für Mineralogie Abhandlungen, 172, 309–323.

Sinmyo, R., Hirose, K., Nishio Hamane, D., Seto, Y., Fujino, K., Sata, N., and Ohishi, Y. (2008) Partitioning of iron between perovskite/postperovskite and ferropericlase in the lower mantle. Journal of Geophysical Research (Solid Earth), 113, B11204.

Solomatova, N.V., Jackson, J.M., Sturhahn, W., Wicks, J.K., Zhao, J., Toellner, T.S., Kalkan, B., and Steinhardt, W.M. (2016) Equation of state and spin crossover of (Mg,Fe)O at high pressure, with implications for explaining topographic relief at the core-mantle boundary. American Mineralogist, 101, 1084–1093.

Struzhkin, V.V., Mao, H.-K., Hu, J., Schwoerer-Böhning, M., Shu, J., Hemley, R.J., Sturhahn, W., Hu, M.Y., Alp, E.E., Eng, P., and others. (2001) Nuclear inelastic X-ray scattering of FeO to 48 GPa. Physical Review Letters, 87, 255501.

Sturhahn, W. (2001) Phase problem in synchrotron Mössbauer spectroscopy. Physical Review B, 63, 124.

——— (2015a) MINUTI (MINeral physics UTIlities). Open source software, http://www.nrixs.com.

——— (2015b) CONUSS (COherent NUclear resonant Scattering by Single crystals). Open source software, http://www.nrixs.com.

Sun, D., Helmberger, D.V., Jackson, J.M., Clayton, R.W., and Bower, D.J. (2013) Rolling hills on the core–mantle boundary. Earth and Planetary Science Letters, 361, 333–342.

Thorne, M.S., and Garnero, E.J. (2004) Inferences on ultralow-velocity zone structure from a global analysis of SPdKS waves. Journal of Geophysical Research, 109, B08301.

Toellner, T.S. (2000) Monochromatization of synchrotron radiation for nuclear resonant scattering experiments. Hyperfine Interactions, 125, 3–28.

Tschauner, O., Ma, C., Beckett, J.R., Prescher, C., Prakapenka, V.B., and Rossman, G.R. (2014) Discovery of bridgmanite, the most abundant mineral in Earth, in a shocked meteorite. Science, 346, 1100–1102.

Van der Hilst, R.D., De Hoop, M.V., Wang, P., Shim, S.H., Ma, P., and Tenorio, L. (2007) Seismostratigraphy and thermal structure of Earth's core-mantle boundary region. Science, 315, 1813–1817.

Welberry, T.R., and Christy, A.G. (1997) Defect distribution and the diffuse X-ray diffraction pattern of wustite, Fe$_{1-x}$O. Physics and Chemistry of Minerals, 24, 24–38.

Wen, L. (1998) Ultra-low velocity zones near the core-mantle boundary from broadband PKP precursors. Science, 279, 1701–1703.

Westrenen, W.V., Li, J., Fei, Y., Frank, M.R., Hellwig, H., Komabayashi, T., Mibe, K., Minarik, W.G., Orman, J.A.V., Watson, H.C., and others. (2005) Thermoelastic properties of (Mg$_{0.64}$Fe$_{0.36}$)O ferropericlase based on in situ X-ray diffraction to 26.7GPa and 2173K. Physics of the Earth and Planetary Interiors, 151, 163–176.

Wicks, J.K., Jackson, J.M., and Sturhahn, W. (2010) Very low sound velocities in iron-rich (Mg,Fe)O: Implications for the core-mantle boundary region. Geophysical Research Letters, 37, L15304.

Wicks, J.K., Jackson, J.M., Sturhahn, W., Zhuravlev, K.K., Tkachev, S.N., and Prakapenka, V.B. (2015) Thermal equation of state and stability of (Mg$_{0.06}$Fe$_{0.94}$)O. Physics of the Earth and Planetary Interiors, 249, 28–42.

Wicks, J.K., Jackson, J.M., Sturhahn, W., and Zhang, D. (2017) Sound velocity and density of magnesiowüstites: Implications for ultralow-velocity zone topography. Geophysical Research Letters, 44, 2148–2158.

Williams, Q., Revenaugh, J., and Garnero, E. (1998) A correlation between ultra-low basal velocities in the mantle and hot spots. Science, 281, 546–549.

Zha, C.-S., Mao, H.-K., and Hemley, R.J. (2000) Elasticity of MgO and a primary pressure scale to 55 GPa. Proceedings of the National Academy of Sciences, 97, 13494–13499.

Zhang, L., and Fei, Y. (2008) Melting behavior of (Mg,Fe)O solid solutions at high pressure. Geophysical Research Letters, 35, L13302.

Zhang, D., Jackson, J.M., Zhao, J., Sturhahn, W., Alp, E.E., Toellner, T.S., and Hu, M.Y. (2015) Fast temperature spectrometer for samples under extreme conditions. Review of Scientific Instruments, 86, 013105.

Zhang, D., Jackson, J.M., Zhao, J., Sturhahn, W., Alp, E.E., Hu, M.Y., Toellner, T.S., Murphy, C.A., and Prakapenka, V.B. (2016) Temperature of Earth's core constrained from melting of Fe and Fe$_{0.9}$Ni$_{0.1}$ at high pressures. Earth and Planetary Science Letters, 447, 72–83.

Zhuravlev, K.K., Jackson, J.M., Wolf, A.S., Wicks, J.K., Yan, J., and Clark, S.M. (2010) Isothermal compression behavior of (Mg,Fe)O using neon as a pressure medium. Physics and Chemistry of Minerals, 37, 465–474.